Key Points:
- The interplay of pore-scale heterogeneity, wettability, and surface roughness controls displacement patterns and capillary trapping efficiency
- The invasion pattern for capillary flow were visualized by micro-CT- and micromodel experiments and classified in a new phase diagram
- Four generic flow regimes (phases) were observed: frontal advance, wetting and drainage invasion percolation, and ordinary percolation

Author Contributions:

Conceptualization: Helmut Geistlinger
Formal analysis: Helmut Geistlinger, Steffen Schlueter
Funding acquisition: Helmut Geistlinger, Mohd Amro
Investigation: Saeed Golmohammadi, Bilal Zulfiqar, Matthias Kuechler, Danny Reuter, Steffen Schlueter
Methodology: Helmut Geistlinger
Project administration:
Helmut Geistlinger, Mohd Amro
Resources: Helmut Geistlinger, Matthias Kuechler, Danny Reuter

A New Phase Diagram for Fluid Invasion Patterns as a Function of Pore-Scale Heterogeneity, Surface Roughness, and Wettability

Helmut Geistlinger[1,2] [ID], **Saeed Golmohammadi[2]** [ID], **Bilal Zulfiqar[1,2]**, **Matthias Kuechler[3]** [ID], **Danny Reuter[3,4]** [ID], **Steffen Schlueter[1]**, **Enrico Segre[5]** [ID], **Ran Holtzman[5]** [ID], and **Mohd Amro[2]**

[1]Helmholtz Centre for Environmental Research-UFZ, Halle (Saale), Germany, [2]Technical University Bergakademie Freiberg, Freiberg, Germany, [3]Fraunhofer ENAS, Chemnitz, Germany, [4]Center for Microtechnologies, Technical University Chemnitz, Chemnitz, Germany, [5]Centre for Fluid and Complex Systems, Coventry University, Coventry, UK

Abstract Understanding how different flow patterns emerge at various macro- and pore scale heterogeneity, pore wettability and surface roughness is remains a long standing scientific challenge. Such understanding allows to predict the amount of trapped fluid left behind, of crucial importance to applications ranging from microfluidics and fuel cells to subsurface storage of carbon and hydrogen. We examine the interplay of wettability and pore-scale heterogeneity including both pore angularity and roughness, by a combination of micro-CT imaging of 3D grain packs with direct visualization of 2D micromodels. The micromodels are designed to retain the key morphological and topological properties derived from the micro-CT images. Different manufacturing techniques allow us to control pore surface roughness. We study the competition between flow through the pore centers and flow along rough pore walls and corners in media of increasing complexity in the capillary flow regime. The resulting flow patterns and their trapping efficiency are in excellent agreement with previous μ-CT results. We observe different phase transitions between the following flow regimes (phases): (a) Frontal/compact advance, (b) wetting and drainage Invasion percolation, and (c) Ordinary percolation. We present a heterogeneity-wettability-roughness phase diagram that predicts these regimes.

1. Introduction

Understanding the complex patterns formed through the displacement of one fluid by another in porous materials is a fascinating scientific problem, one which is also key in a wide range of natural and engineering applications across scales, from sub-mm microfluidics to km-scale water and energy resources. The displacement patterns vary widely from compact fronts to being highly ramified where the flow advances along preferential flow paths (fingers, Lenormand et al., 1988). The displacement characteristics in terms of how much of the original fluid is swept versus how much is trapped behind, and how convoluted the interface is between the fluids, is of great economic value. In some applications, such as carbon geosequestration and soil remediation, ramified displacement is desirable as it provides greater interfacial area and hence stronger mixing and reactions. In others, the opposite is true. Examples include manufacturing of materials or coatings where uniformity enhances the appearance and strength, or hydrocarbon recovery which relies on efficient displacement leaving as few hydrocarbons as possible in place (Juanes et al., 2020).

Numerous experimental and theoretical studies have investigated how the intricate interactions between the properties of the fluids, the solid pore surfaces, and the microstructure, that is, the grain and pore geometry and their topology, affect the resulting patterns, displacement efficiency, and trapping efficiency.

A deeper understanding of the complex flow patterns has been achieved in the last 10 years by μ-CT experiments in artificial glass sphere sediments (glass beads), sand and sandstone (AlRatrout et al., 2018; Andrew et al., 2014b; Armstrong & Wildenschild, 2012; Herring et al., 2016; Wildenschild et al., 2011).

There are conflicting experimental and numerical results on the effects of wettability on trapping efficiency in capillary flow (Akbarabadi & Piri, 2013; Andrew et al., 2014a; El-Maghraby & Blunt, 2013; Herring et al., 2016; Hu et al., 2017; Iglauer et al., 2012; Jung et al., 2016; Pentland et al., 2011; Rahman et al., 2016; Singh et al., 2017; Trojer et al., 2015). Some authors considered that surface chemistry (wettability) plays a central role in trapping, while others, such as (Andrew et al., 2014b), concluded that differences in rock chemistry (at least under conditions of chemical equilibrium) are less important for the overall dynamics of ganglia/clusters than differences in

Software: Matthias Kuechler, Steffen Schlueter, Enrico Segre, Ran Holtzman
Supervision: Helmut Geistlinger, Mohd Amro
Validation: Helmut Geistlinger, Steffen Schlueter
Visualization: Saeed Golmohammadi, Bilal Zulfiqar, Matthias Kuechler
Writing – original draft: Helmut Geistlinger
Writing – review & editing: Ran Holtzman

pore structure and connectivity. Andrew et al. (2014b) studied five different rock types (Bentheimer and Doddington sandstone; Estaillades, Ketton, and Mt Gambier carbonate) under reservoir condition (50°, 10 MPa) at low capillary numbers of 10^{-6} using μ-CT with high resolution (6 μm). The porous rocks are characterized by a highly irregular and well-connected pore space, as illustrated by the cross-sections and 3D images (Figures 2.3 and 2.4 in Blunt (2017)). The pore wall surfaces show high wall roughness and microporosity (Figure 2.7 in Blunt (2017)). The most striking result was that all rocks show a similar and significant trapping efficiency of scCO$_2$, that is, the ratio of residual and initial saturation, about two third of the initial saturation. Comparing connectivities averaged over pore volume (7, 6, 5, 5, 21) with trapping efficiencies (0.71, 0.70, 0.65, 0.65, 0.66), one comes to the unexpected conclusion that the two are not correlated, and that the topology of the pore space has no effect on trapping. This is difficult to understand. Actually, one would expect the two to be negatively correlated, that is, higher connectivity leads always to lower trapping efficiency because the defending fluid can escape more easily in porous media with high connectivity. Interestingly, the cluster size distributions of all rock samples except the Mt. Gambier carbonate follow a power law with an exponent close to the universal scaling exponent 2.19, suggesting that the displacement process is percolation-like.

One possible reason for the contradictory and sometimes incomprehensible experimental results is the neglect of pore wall roughness. Porous media with similar Minkowski functions but different degrees of surface roughness show a significant difference in capillary trapping, as we have shown by μ-CT experiments (Geistlinger et al., 2015). An extreme example of the influence of surface roughness is discussed in Geistlinger et al. (2016) and shown in Figure 1. Visualization experiments of a quasi-2D microstructure consisting of random cylinders of the same size and having a rough surface show that an advancing/pre-wetting thick-film flow (TFF) triggers efficient snap-off trapping, where the cluster size distribution obeys a universal power law according to *Ordinary Percolation* (*OP*) with trapping. Figure 1b shows the trapped clusters of the defending fluid (blue). The identical smooth surface microstructure exhibits compact displacement, that is, FA, without trapping (Figure 1a, invading fluid: black).

Based on numerical simulations and experimental static fluid patterns (CT experiments), Blunt (2017) proposed a "heterogeneity versus wettability" phase diagram to classify the fluid patterns in porous media with smooth and rough surfaces for the capillary flow region (see Figure 4.21 in Blunt (2017)). The phase diagram recognizes the importance of *TFF* (also called layer flow) and corner flow (CF) through crevices and corners in rough, angular pores, which are inherent for natural porous media such as sand and sandstone. We note that thick-film and CF are not present in smooth PDMS structures studied by Xu et al. (2014). Since the contact angle of this micromodel study is 110° > 45° (critical contact angle for CF), CF is not possible.

We note that the phase diagram proposed by Blunt (2017) has not yet been experimentally verified by the visualization of dynamic flow patterns. This is also stated by Blunt (2017): "To date, there is no direct experimental confirmation of this phase diagram through visualization experiments."

Of particular interest is the interaction of heterogeneity of pore size and wettability on the efficiency of capillary trapping. The term "pore-scale heterogeneity" is introduced here as a qualitative measure by comparing the capillary threshold pressures in throats with those of cooperative filling. Intuitively, sand, and sandstone exhibit a higher degree of pore-scale heterogeneity/disorder than uniform, densely packed glass spheres. Theoretically, for a completely regular structure, for example, packed glass spheres of equally sized spherical grains, a single advance leads to complete filling: this is a frontal advance (FA), independent of the (homogeneous) contact angle (Geistlinger & Ataei-Dadavi, 2015). In a more heterogeneous porous medium such as sand with irregularly shaped grains and a wide range of pore sizes, the advance becomes invasion percolation regardless of the contact angle, as the invasion is solely controlled by the pore size and not by the cooperative filling.

Our new phase diagram, shown in Figure 2, is based on experimental visualizations of the dynamic flow patterns for a variety of microstructures:
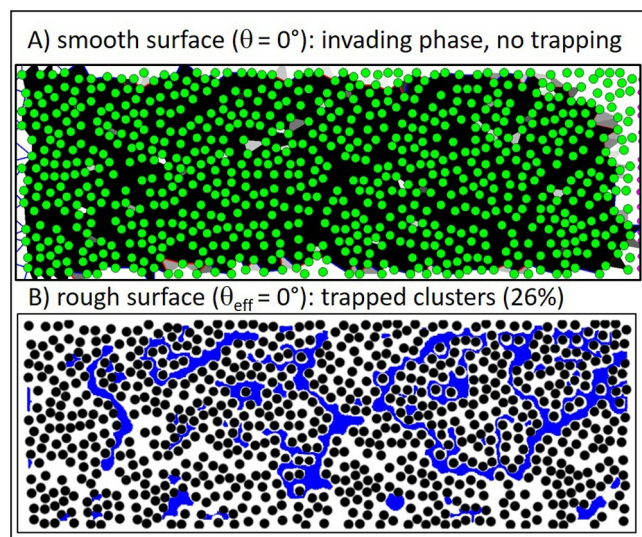

Figure 1. Under strong imbibition (complete wetting) capillary flow for a 2D microstructure with equalized circular grains follows compact frontal advance when its surface is smooth (a) and Ordinary percolation with maximum trapping when its surface is rough (b). (a) Shows the black invading fluid (CR-modeling, Cieplak & Robbins, 1990) and (b) shows the trapped clusters (blue) of the defending fluid (experimental results, Geistlinger et al., 2016).
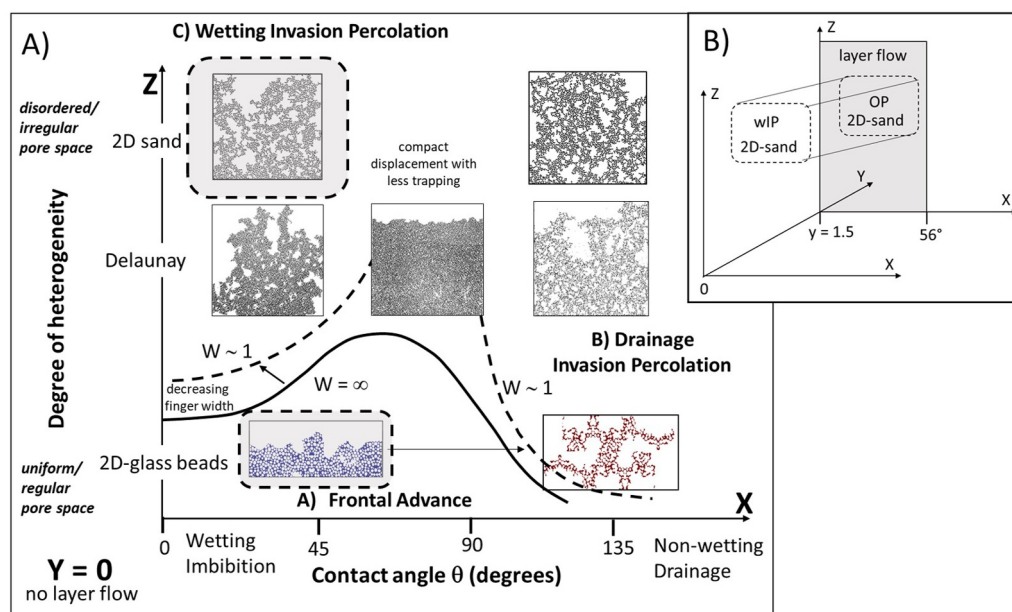
Figure 2. (a) Phase diagram for porous media with smooth surfaces ($y = 0$): The phase diagram shows the transition in flow regimes from (a) frontal advance to (b) drainage invasion percolation with increasing contact angle and for uniform porous media (2D glass beads). For porous media with higher heterogeneity/disorder and smooth surface (Delaunay pore structure, 2D sand) a second transition to wetting invasion percolation (wIP) is observed. The transitions in displacement regimes are quantified by the finger width, W. (b) Phase diagram for porous media with rough surfaces ($y = 1.5$): The schematic, three-dimensional phase diagram shows the phase transition for 2D sands (shaded area in a) from wIP to ordinary percolation with trapping. The $y = 1.5$ plane characterizes the roughness of glass-ceramic micromodels and the shaded area the contact angle region where spontaneous thick film flow occurs (complete wetting).

regular, irregular, statistically representative, Delaunay microstructures with medium degree of disorder, microstructures with increasing degree of disorder, CT cross-sections. In addition, the new phase diagram is based on CT measurements in glass bead packings (porous media with a low degree of disorder) and sands (porous media with a high degree of disorder).

In contrast to Blunt (2017), we consider larger capillary numbers $Ca \approx 10^{-6}$. As before, the viscous forces are negligible, but the thick film and CF is now followed at some distance (several pore diameters) by bulk flow. The immediate consequence is that "growth" of wetting clusters is not possible. Experimental flow patterns in 2D glass spheres (and also in 3D glass spheres; CT measurements) show a compact displacement front with less precursor CF.

The 3D-phase diagram (Figure 2) shows different generic flow regimes (displacement regimes, phases) depending on the wettability (contact angle, x-axis), the surface roughness (y-axis) and the heterogeneity/disorder (z-axis) of the pore structure. The roughness is defined as the ratio of rough to flat surface.

Porous media with smooth surfaces ($y = 0$): Figure 2a shows three generic flow regimes for porous media with smooth surfaces (a) FA (b) wetting invasion percolation (wIP) and (c) drainage invasion percolation (dIP).

Porous media with rough surfaces ($y > 0$): As we will show below, glass-ceramic micromodels have a roughness of $y = 1.5$, which always leads to complete wetting, that is, layer flow, at contact angles smaller than 56°. The area where spontaneous layer flow is possible is shaded gray on the $y = 1.5$ plane in Figure 2b. The x–z region shaded in Figure 2a, which is projected onto the $y = 1.5$ plane in Figure 2b, characterizes the heterogeneity and wettability of 2D sands. For the first time, we have experimentally observed the interesting phase transition from wIP ($y = 0$) to OP ($y > 0$) for 2D sands with identical pore structure but different roughness, that is, different y-values. According to this phase diagram, a phase transition from FA (compact displacemnt) to OP with trapping is expected for 2D glass beads (low heterogeneity/disorder). This was experimentally demonstrated in Geistlinger et al. (2016) and is shown in Figure 1.

As in the classical phase diagram of Lenormand and Zarcone (1985), we show the experimental flow patterns of each phase in each quadrant of the phase diagram and derive the phase boundaries; $W \approx 1$ or $W \to \infty$, by applying the percolation laws. A detailed discussion is given in Supporting Information S1.

Earlier works, for example, Lenormand and Zarcone (1984) and Blunt (2017) that considered the effect of TFF and CF, assumed that the pore space can be described by a straight, continuous capillary with angular rough cross section and assumed the existence of a connected, continuous film network, respectively, that is, high connectivity of small throats such that (a) unilateral films can reach the other side of the throat (geometric snap-off condition, Golmohammadi et al., 2021; Zhao et al., 2016) and that (b) precursor films can extend over larger areas of the porous medium such that trapping can occur. However, rough surfaces of sandstones (Figure 2.7 in Blunt (2017) or glass ceramics (Geistlinger et al., 2015)) exhibit a disordered micro-porous structure of interrupted grooves and crevices along the inner pore walls, that could void these assumptions.

μ-CT experiments have two limitations: (a) the resolution of 6–15 μm does not allow direct observation of the *TFF*, also called layer flow, which has a typical thickness of 10 μm, and (b) the reconstructed 3D images show only static fluid-fluid patterns. Therefore, visualization experiments with micromodels (2D) are performed to investigate the flow dynamics accepting that the two-phase bi-continuity of 3D-porous media (Adler & Brenner, 1988; Wilkinson, 1984) cannot be transformed/mapped onto 2D porous media (Anbari et al., 2018; Gogoi & Gogoi, 2019; Haghighi et al., 1994; Karadimitriou & Hassanizadeh, 2012).

An interesting microstructure whose capillary flow pattern and trapping behavior has not been studied before is the Delaunay structure (Delaunay, 1934; Karadimitriou & Hassanizadeh, 2012). In this paper we presented new experimental results for the Delaunay microstructure, which exhibits similar porosity, connectivity, and throat size distribution as Berea sandstone using Delaunay Triangulation. The microstructure looks like a random mesh with varying coordination number (Figure S3 in Supporting Information S1).

The paper is organized as follows, we briefly describe the experimental methodology, then we discuss the theoretical basis. In the results-discussion section, we first discuss previous μ-CT experiments (3D) (Zulfiqar et al., 2020) where we assume that the precursor TFF and CF control the trapping process. We performed visualization experiments with 2D micromodels to investigate the dynamics of the TFF and CF. For smooth pore wall surfaces, and uniform pore structures, for example, glass beads, we found that trapping decreases with contact angle (from imbibition to drainage). Increasing the pore-scale heterogeneity, for example, the pore angularity, we found a nonmonotonic dependence of trapping on wettability: maximal trapping in imbibition, decreasing to a minimum at neutral wettability and increasing again in drainage. This corresponds to a phase transition from wetting IP to drainage IP, with about the same trapping efficiency. Rough wetting pore walls doubles the trapping efficiency comparing identical pore structures. The Delaunay microstructure shows this nonmontonic behavior in trapping efficiency. Using these experimental results, we verify the proposed phase diagram - at least parts of it.

2. Materials and Methods

2.1. 2D Micromodel Experiments

To explore a wide range of microstructures and wetting conditions experimentally, we use different types of media and fluids. The media differ by both the method of generating the pore space geometry, that is, the theoretical procedure to design the pore size and shape, and the manufacturing procedure which controls the crucial property of pore wall roughness. Below we briefly describe these methodologies (for details see Golmohammadi et al. (2021)).

All experiments were carried out in a horizontal direction and at capillary numbers $Ca = 10^{-6}$ where capillary forces dominate viscous forces. To maintain a constant flow rate during imbibition experiments, a high-precision bidirectional syringe pump with a step resolution of 0.046 microns (Fusion 200, Chemyx, Stanford, USA) was used. For visualization, we used a Canon EOS7D SLR camera with a 100 mm Macro lens in combination with a fluorescence microscope. The experimental setup is shown in Figure 3. Uranin and Oil Red dyes were used as fluorescent tracers. The fluid patterns were analyzed using Fiji/ImageJ (Schindelin et al., 2012).

The contact angle was varied over a range corresponding to imbibition at one extreme to strong drainage at the other by using different fluid-fluid pairs (Singh et al., 2017): (a) $\theta = 38°$: water-air, (b) $\theta = 56°$: glycerin-air, (c),
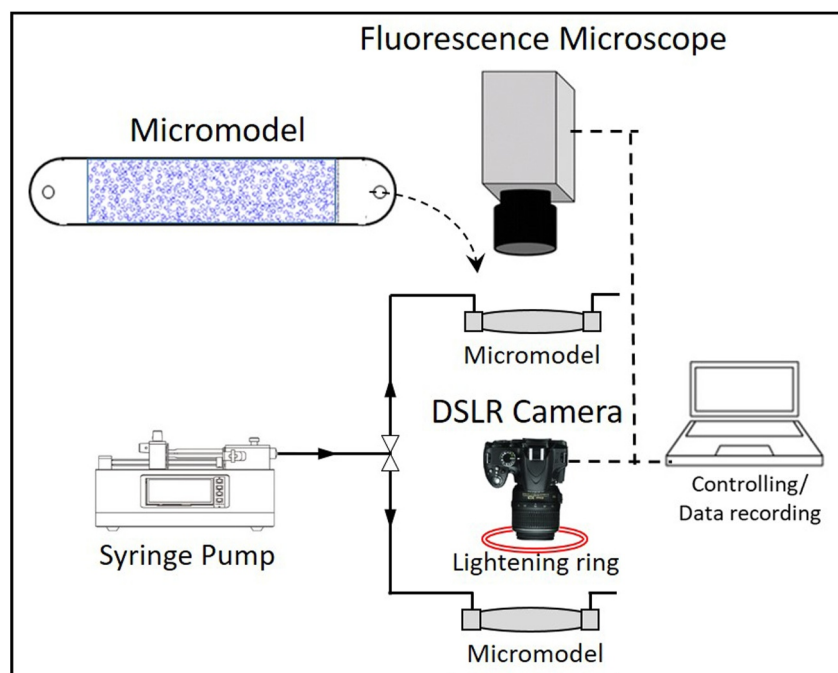
Figure 3. Experimental setup to visualize the flow patterns both with overview mode (REV scale, DSLR camera) and in microscope mode (pore scale).

$\theta = 138°$: heptane-water, and (d) $\theta = 142°$: air-water. When air was the invading fluid, Ca was calculated for the defending fluid. The contact angles are mean values of the PYREX and Si contact angles. The physico-chemical fluid properties are listed in Table S2 in Supporting Information S1.

2.2. Design of Pore Space Geometry

Three main techniques were used to design the pore space geometry: (a) direct geometric mapping (Patsoukis Dimou et al., 2022), (b) topological mapping (Bruecher & Bottlinger, 2006; Golmohammadi et al., 2021; Schlüter et al., 2010), and (c) Delaunay triangulation. The three are designed to capture different aspects of the pore topology and geometry, thus being representative of different features of natural 3D media. The grain and pore size distributions both of the 3D–2D porous media are given in Table S1 in Supporting Information S1.

In the direct geometric mapping, the binary images (masks for the etching process) were generated from micro-CT cross sections of 3D samples of glass beads packs, sand packs, and Bentheimer sandstone (example of the latter is shown in Figure S2 in Supporting Information S1). Then, the cross sections were replicated in flow direction. The dimensions were $20 \times 80 \times 0.1$ mm. Examples are shown in Figure S4 in Supporting Information S1.

For the Delaunay microstructure the algorithm starts to scatter about 16,000 points (nodes) on a 2D plane representing the pore centers, where the Halton method is used to obtain the best spread out avoiding point clumping (Fasshauer, 2007). Then, the Delaunay triangulation is performed using MATLAB. To ensure a homogeneous fluid invasion, 50 points were placed uniformly at each boundary. In the last step, inflow and outflow structures were designed, that is, A cascade of inflow channels on one side and a triangular outlet region on the other side. The etching depth was 100 μm. The x–y-dimensions were 80×80 mm. The Delaunay micromodel is shown in Figure S3 in Supporting Information S1.

2.3. Fabrication of Micromodels

An interval-based ICP-DRIE technology was used for anisotropic etching of silicon wafer (Rabbani et al., 2017; Zuo et al., 2013). This resulted in high edge steepness and a true mapping of the lattice structure with depth. Figure S5a in Supporting Information S1 shows an interesting 3D–2D-transformed pore structure with irregular
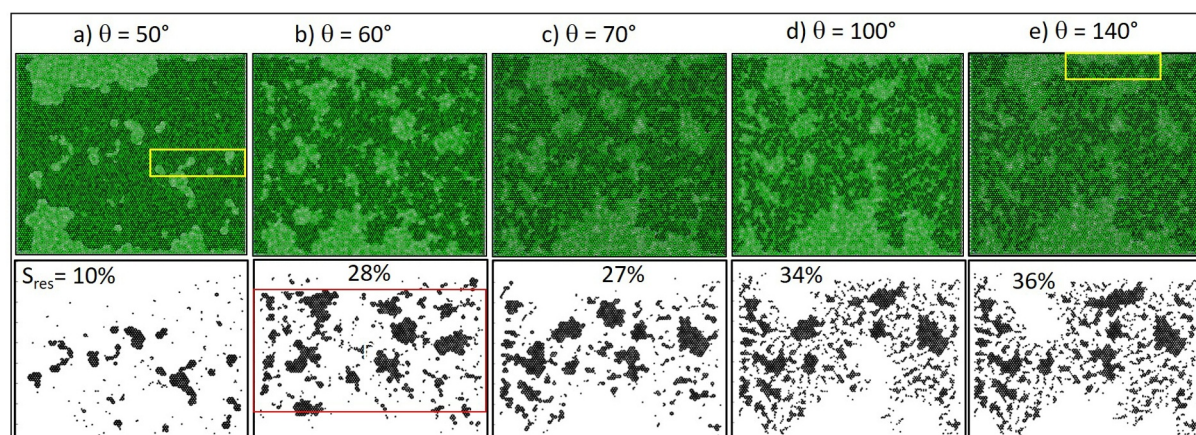
Figure 4. Pore network simulations for 2D glass beads showing contact angle dependency of fluid pattern (top) and trapped clusters (bottom). Contact angle is listed above the top row; residual fluid saturation S_{res} is shown on each inset and normalized by the area of the red rectangle. Yellow rectangles show the dimensions of the micromodel and similar fluid patterns as shown in Figure 8.

shaped grains and smooth pore walls. An identical microstructure was generated using highly accurate anisotropic photolithographic etching of photosensitive glass-ceramic FOTURAN (Schott-GmbH). The main feature of the microstructure is the surface roughness, which is caused by the glass-ceramic (roughness parameter: mean surface height $\delta = 1$ μm, wavelength $\lambda =$ μm; ISO-standard, 1997). For details of the ICP-DRIE and the FOTURAN-etching process, see Golmohammadi et al. (2021). Both microstructures were covered with a plain PYREX-glass plate by thermal diffusion bonding (see Supporting Information S1).

3. Theoretical Background

3.1. Pore Network Model

A brief description of the numerical model used in the simulations is provided below; for further details see Holtzman and Segre (2015) and Zhao et al. (2019). Our model combines the quasistatic approach originally proposed by Cieplak and Robbins (1988) and Cieplak and Robbins (1990) with a single pressure, dynamic model of flow through the pore network. The model considers three types of instability events—burst, touch, and overlap, for which an analytical stability criteria is available for the simple geometry of circular particles. Based on the fluid-fluid interface stability, its advancement (along with the pressure field and flow velocities) is computed considering the viscous resistance in the interconnected network of pores. The interface is represented as a set of cylindric menisci, which touch the posts at an in-plane contact angle θ. The model is effectively 2D in the sense that it considers the in-plane curvature only in computing the meniscus curvature, a reasonable approximation for 3D array of cylindrical pillars (posts) when the out-of-plane curvature is much smaller than the in-plane one (e.g., for post diameters much smaller than their height). Such 2D pore-scale representation cannot capture mechanisms at the sub-pore scale, in particular incomplete filling mechanisms (film or CF). Our model also does not consider snap-off. However, the model simplicity results in a highly computationally efficient code (orders of magnitude faster than other models, see Zhao et al. (2019)), which allows simulations of domains sufficiently large to systematically and reliably explore the impact of pore-scale heterogeneity as well as large data sets with multiple realizations that are required for statistics, parametric exploration, and sensitivity analysis.

3.2. Simulations

Pore network simulations were carried out for three realizations of a statistically representative pore network (10,000 nodes; 20,000 pores) varying contact angles between weak imbibition (50°) to strong drainage (140°). The fluid pattern (top row in Figure 4) show a Cieplak-Robbins (CR)-transition from compact to fractal pattern with little to maximal trapping. The yellow marked sections for normal imbibition (Figure 4a) and strong drainage (Figure 4e) reproduce the experimental pattern (shown in Figures 8a and 8b). For weak imbibition the simulation shows few trapped clusters, which agree reasonable well in size and shape with the experimental ones. For strong drainage the micromodel window (=yellow marked rectangle) captures only one finger of the large (statistically
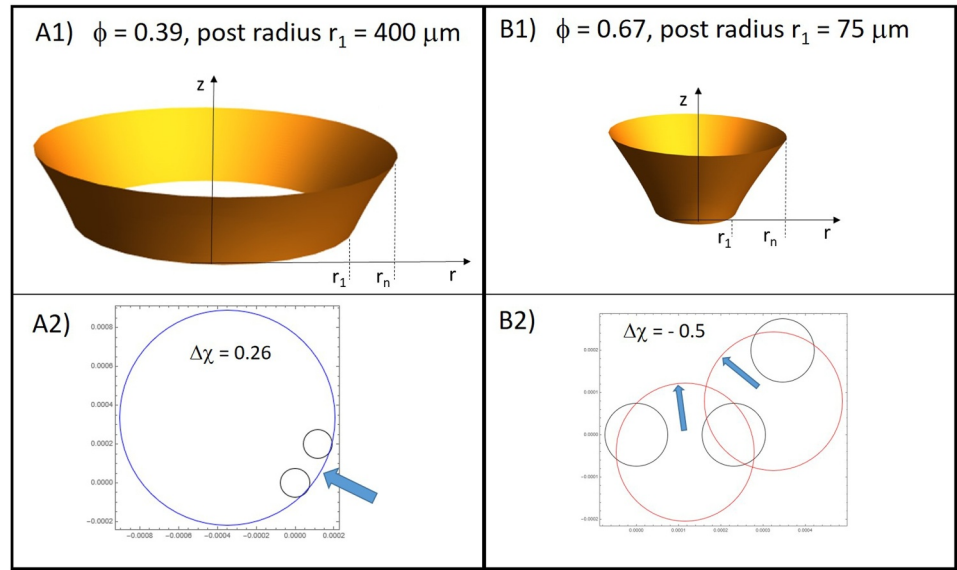
Figure 5. Corner flow around a circular post of radius r_1 for low porosity 2D glass beads (a) and high porosity random cylinders/posts (b) and for imbibition at contact angle $\theta = 38°$. The 3D-figures are magnified in z-direction by a factor 2. The blue circle in Figure 2a and the red circles in Figure 2b show the mean radius of curvature of the interface shown in Figures 1a and 1b. The blue arrows indicate the front advance.

representative) fractal patterns. The spatial distribution of trapped inner clusters that is, boundary clusters were excluded, are shown in the bottom row of Figure 4. The trapping efficiency that is, the residual saturation S_{res} (percentage is shown in Figure 4).

3.3. Precursor Corner Flow

Precursor CF only occurs if it can bridge the critical distance r_n from the post center to the surface of the next neighboring post. The radial dependence $z(r)$ of the CF interface obeys the following differential equation:

$$\frac{\dot{z}}{r(1 + \dot{z})^{1/2}} + \frac{\ddot{z}}{r(1 + \dot{z})^{3/2}} = \frac{\Delta p}{\sigma} \tag{1}$$

where $\dot{z} = dz/dr$ (Section 1.1.5.2 in Gennes PG and Brochard-Wyart (2004), Primkulov et al. (2021)). The Laplace pressure Δp can be calculated from the force balance. For a static interface, capillary forces in z direction have to be balanced by the pressure force thus:

$$2\pi r_n \sigma \sin(\theta) - 2\pi r_1 \sigma \cos(\theta) = \Delta p \pi (r_n^2 - r_1^2) \tag{2}$$

where r_1 denotes the post radius. The ratio of the Laplace pressure and the interface tension σ gives the curvature C of the interface

$$\frac{\Delta p}{\sigma} = \frac{1}{R_1} + \frac{1}{R_2} = C = \frac{1}{R} \tag{3}$$

where $1/R_1$ denotes the positive concave curvature C_1 along the interface profile $z(r)$ (Figures 5a1 and 5b1), $1/R_2$ denotes the negative convex curvature C_2 around the post, and $1/R$ the mean curvature C. Physically, the two curvatures compete each other. The numerical solution of 1 for 2D glass beads ($r_1 = 400$ μm, porosity $= 0.39$, $\theta = 38°$, $\sigma = 72$ mN/m) yields a critical distance of 110 μm, about 1/8 of the grain diameter and a Laplace pressure of 3 Pa. Geometrically, it means that the mean curvature of the corner meniscus is approximately zero and the duct flow meniscus between neighboring grains is flat. Hence, overlap is not possible and precursor CF is favored over
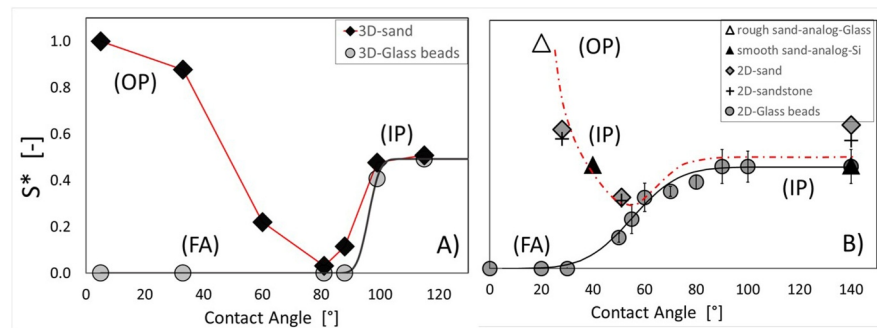
Figure 6. Non-monotonous contact angle dependency (red lines) of the normalized trapped saturation of the defending fluid S^*, in both 3D micro-CT images (a; normalized by $S_{norm} = 13\%$) and 2D micromodel experiments (b; $S_{norm} = 73\%$). Glass beads data in both 2D and 3D (circles) was fitted to an error function, indicating the CR transition from frontal advance to Invasion Percolation. In 3D sand and 2D sand-analogs (rough surface), the more efficient snap-off trapping is caused by spontaneous thick-film water flow during imbibition. Reduced phase connectivity in 2D enhanced trapping, for example, minimum value increases from zero in 3D to ~0.2. Increased grain angularity also increases trapping; for example, compare 2D smooth micromodel analogs of sand versus glass beads (b).

compact displacement indicated by a positive $\Delta\chi$ value of 0.26 (Figure 5a2, $\Delta\chi$-overlap criterion see Holtzman & Segre (2015)). In realistic 3D glass bead packs there are always paths of grain-grain contacts. Along these paths, grain-grain bridging occurs in 2D glass beads shown in Figure 9a. For a high-porosity microstructure with random cylinders ($r_1 = 75$ μm, porosity = 0.67, $\Delta p = -284$ Pa) the convex neighboring menisci overlap indicated by a negative $\Delta\chi$ value of -0.5 (Figure 5b2). Hence, compact displacement is favored over precursor CF (see Figure 9b).

4. Results and Discussion

If water flows very slowly into air-saturated glass bead packs at imbibition, the displacement front is compact due to cooperative filling as our μ-CT experiments showed (Geistlinger & Zulfiqar, 2020). Trapping is unlikely to occur (Figure 6a, circles), because air can escape through continuous paths (bi-phase continuity (Adler & Brenner, 1988; Wilkinson, 1984)). The displacement regime in the phase diagram is FA. Within a narrow θ range (90°–100°, critical contact angle $\theta_c = 96°$), the trapping efficiency ($S^* = S_{res}/S_{norm}$, residual saturation S_{res} normalized by $S_{norm} = 13\%$) changed drastically from zero to maximal trapping. This transition, also denoted as the "Cieplak-Robbins (CR) transition" (Cieplak & Robbins, 1990), is characterized by a substantial, qualitative ("phase") change. For $\theta > \theta_c$ the displacement occurs by IP. Finger width W decreases from FA to IP, where $W \sim 1$ determines the critical contact angle (Figure 2; in agreement with Cieplak and Robbins (1990)). The number of large trapped clusters exhibits universal scaling (Wilkinson, 1984): $n(s) \sim s^\tau$, where s is the numbers of pores, with universal scaling exponent of $\tau = 2.19$ in 3D (Geistlinger & Zulfiqar, 2020).

Studying the water-air displacement process in sand packs with similar/identical topological measures as those of glass bead packs (similar Minkowski functions, Geistlinger et al., 2015), we expect a similar trapping behavior. This is the case for strong drainage ($\theta > 100°$; filled diamonds in Figure 6a), where the displacement regime is dIP. For strong imbibition (hydrophilic grains), the 3D sand shows unexpected maximum trapping, approximately twice that of the drainage case. This may be attributed to efficient snap-off trapping due to precursor TFF and CF in porous media with rough and angular grains. The displacement regime is now *OP* with trapping.

We hypothesize that the observed high trapping efficiency in sands is due to efficient snap-off trapping resulting from TFF and CF along the rough pore walls. A partial support for this hypothesis is provided by micro-CT images, showing that in imbibition a thick water films cover the sand grains and suggesting that the trapped air clusters are completely surrounded by a closed spherical interface (see Figure 7a), versus partial cover by convex interface in drainage (Figure 7b). To test this hypothesis, we visualize the displacement in the 2D micromodels which replicate the 3D packings topology. We find the following behavior in each of the mediums tested.

(i) The 2D glass beads micromodel exhibits a similar phase transition as its 3D counterpart from compact or FA to dIP fractal pattern (Figures 2 and 8a–8c), with increased trapping efficiency from minimal to maximal
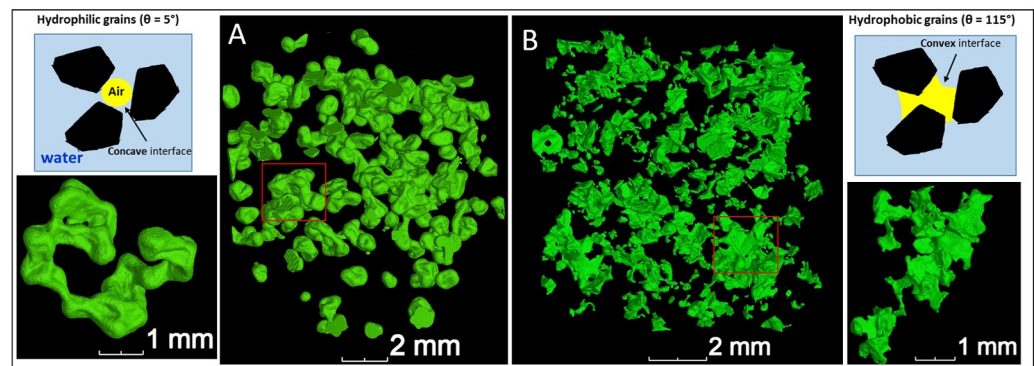
Figure 7. μ-CT images of trapped air clusters, showing a change in curvature sign from spherical concave (positive curvature) in hydrophilic sand ($\theta = 5°$, a) to convex (negative curvature) in hydrophobic sand ($\theta = 115°$, b) sands. This results from different invasion and trapping mechanisms. (a) Spontaneous thick film flow causes snap-off trapping and (b) duct flow causes bypass trapping.

trapping (Figure 6b). We note a few quantitative differences: in 2D, the range of contact angles where the transition occurs is larger, 40°–80°, with a different critical value, $\theta_c \sim 60°$ (Figure 6). Also, as 2D limits connectivity of defending phase, trapping is enhanced: 0.06–0.13 for $\theta = 38°$–56°. The dependence of trapping upon the contact angle for round smooth grains (e.g., glass beads, not accounting for TFF and CF), namely the CR transition, was computed using a pore network model in Holtzman and Segre (2015) (see Figure 4).

(ii) In contrast to idealized porous media with circular posts, 2D sand and sandstone show ramified/fractal displacement fronts and trapping at imbibition, which characterizes wIP. In the phase diagram (Figure 2a) this transition from FA to wetting IP occurs with increasing heterogeneity/disorder. Figure 8 (sand: second row d–f; sandstone: third row g–i) shows the fluid pattern at breakthrough and (Figures 9c and 9d) show the fractal displacement front of sandstone and sand, respectively at pore scale. The trapping efficiency exhibits a similar non-monotonic behavior as 3D sand with a maximum of ∼40% at imbibition ($\theta = 38°$) and at strong drainage ($\theta = 140°$; diamonds and crosses in Figure 6b). It is interesting to note that the minimum trapping efficiency is ∼20% and not zero as with 3D sand, showing once again that trapping in 2D is more likely than in 3D.

(iii) Delaunay microstructure: The flow patterns show a similar phase transition as in sand and sandstone, that is, from wetting IP to compact FA and to draining IP with the typical non-monotonic trapping behavior from 13% to 2%, and then to 32% (compare Figure 10 with Figure 2a). Thus, it reflects the main characteristic of trapping in natural porous media. Figure 9f shows a trapped cluster surrounded by filled throats. The inner throats are covered by CF. Interestingly, snap-off is rather seldom and happens not inside the straight rectangular throats, because the capillary snap-off pressure in a straight quadratic duct with width a is only half of the capillary pressure of the piston meniscus $4\sigma/a$, $\theta = 0°$, that is, duct flow is always favored over snap-off. This is the reason for the small trapping efficiency of 13% compared to sand and sandstone. In conclusion, the Delaunay microstructure describes qualitatively the θ-dependence of the trapping behavior, but underestimates the trapping during imbibition.

As shown in Video S1, the dynamics of the front advance and the bypass trapping are controlled by precursor CF with unstable grain-grain bridging (snap-off events) and subsequent duct flow (see also Figures 9c and 9d). This efficient snap-off trapping leads to maximum trapping efficiency during imbibition. The comparison of 2D glass beads and the Delaunay microstructure, on one side, with 2D sand and sandstone, on the other side, shows that irregular grain shape, that is, pore-scale heterogeneity/disorder, amplifies trapping during imbibition. Consequently, the irregular (conical) throat geometry determines whether grain-grain bridging (snap-off) occurs and the front advance is driven by precursor CF, or whether grain-grain bridging is hindered and the front advance is driven by duct flow.

Increasing the contact angle from 38° to 56° makes the flow pattern for all 2D porous media more compact, and they can classified as FA with less trapping. In this transition range (see Figure 2) the trapping behavior of sand and sandstone changes qualitatively from snap-off trapping to bypass trapping, with the trapping efficiency
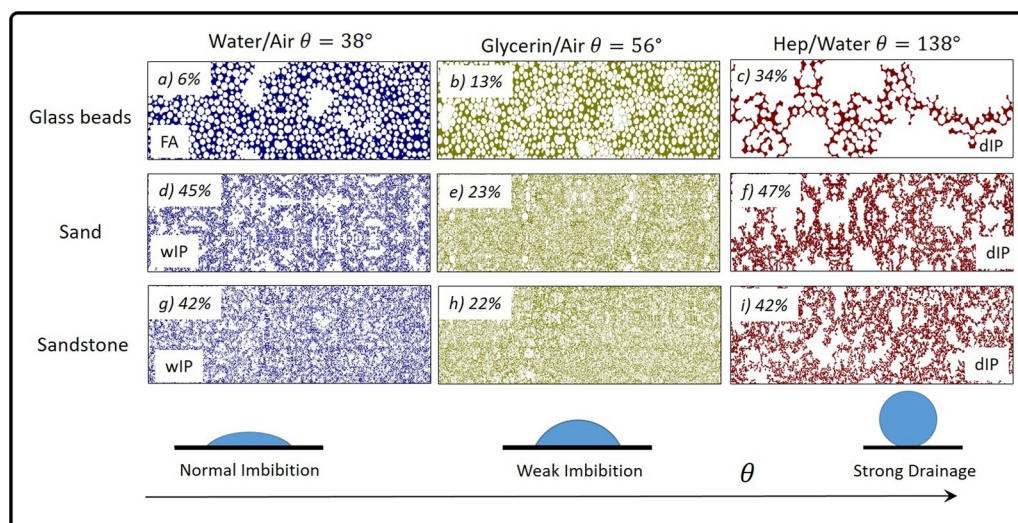
Figure 8. Macroscopic displacement patterns and trapping efficiency (residual saturation, in %) at breakthrough as function of wettability for micromodels of increasing degrees of pore space heterogeneity: Rows 1–3 are 2D cross sections from glass bead packs, sand and sandstone, respectively. The invading fluid is colored, defending fluid and solid matrix not shown (white). The imbibition patterns (first column) show that with increasing pore space heterogeneity a transition from frontal advance to wetting wetting invasion percolation takes place. For neutral wettability (second column) all porous media show compact displacement and less trapping (transition range in Figure 2) compared to that of drainage drainage invasion percolation (last column).

reduced by approximately 50%. Increasing the contact angle further to $\theta = 140°$ (strong drainage) increases trapping and it again reaches its starting maximum. The trapping is now triggered by core annular flow (see Video S1). The flow regime is always IP and can be described by the phase diagram without TFF ($y = 0$), but the trapping mechanism changes from CF-controlled snap-off trapping to duct-flow-controlled by-pass trapping with increasing contact angle.
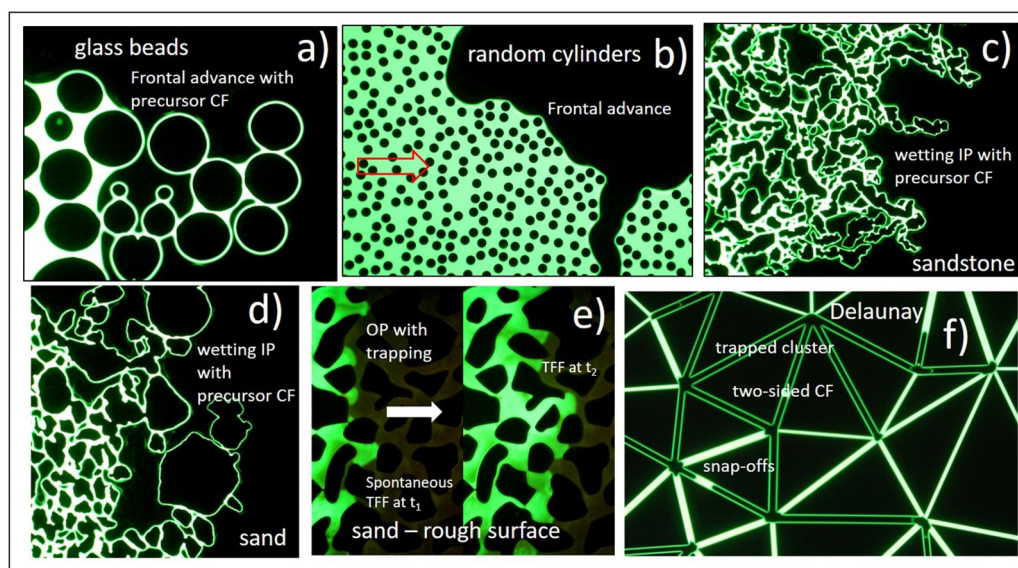

Figure 9. Microscopic wetting mechanisms captured with fluorescent microscope imaging: (a) Precursor corner flows (green rings around the front grains) in 2D glass beads (low porosity = 0.39) with smooth surface in imbibition ($\theta = 38°$, see Figure 8a). Bright pores are completely filled by duct flow or by grain-grain bridging (snap-offs); (b) random cylinders (high porosity = 0.67) compact frontal advance; (c, d) wetting Invasion Percolation with precursor CF in sandstone and sand, respectively; (e) Spontaneous thick-film flow at subsequent times (marked t_1 and t_2) in 2D sand analogs made of glass ceramics (rough surfaces); (f) trapped cluster in Delaunay microstructure. In all panels, water displaces air from left to right.
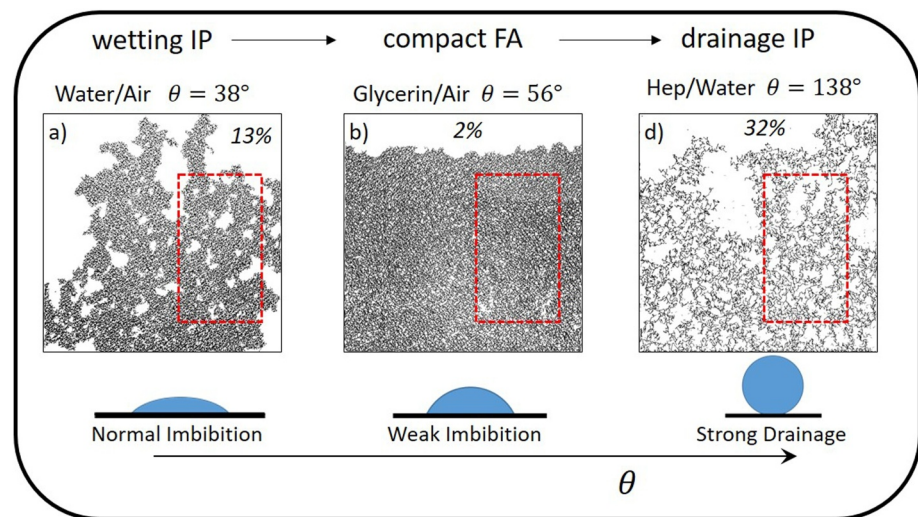
Figure 10. Fluid-fluid pattern for the Delaunay microstructure. Experiments carried out at $Ca = 10^{-6}$, stopped at breakthrough. The contact angle was varied here by changing the fluid pair; the invading fluid is black, defending fluid and solids not shown (white). The residual saturation is measured in the red window and shown as a percentage.

The front dynamics shown in the video for strong drainage in 2D-sands are discontinuously similar to that described by Furuberg et al. (1988). Once a new pore was invaded, the front tended to stay in that vicinity. The growth during a short time interval tends to occur within a region of connected large pores. Qualitatively, this can be understood: The invading front exhausts all easily invaded pores, then by forcing the invader through a difficult pore a new region, which may have new easily invaded areas, is made available to the front. The front then moves into this area until it gets stuck again having exhausted the new easily invaded pores.

The key question is why the trapping efficiency for 3D sand is doubled for strong imbibition compared to strong drainage (diamonds in Figure 6). Note that 2D sand and sandstone show a symmetrical trapping behavior (diamonds and crosses in Figure 6b). Following Wenzel's argument (Blunt, 2017; Wenzel, 1936) that surface roughness amplifies the intrinsic wettability, that is, hydrophilicity and also hydrophobicity is amplified, we hypothesize that the different wetting behavior on rough surfaces causes this different trapping behavior.

Visualization experiments with 2D sand analogs, that is micromodels with identical microstructure but different degrees of surface roughness, support this hypothesis. The micromodel with rough surface (Figure 6b, empty triangle) yields a residual air saturation of 73% that is, nearly doubled that of the micromodel with a smooth surface (Figure 6b, full triangle, $S_{res} = 34\%$). The video shows that spontaneous precursor water flow occurs on the rough siliceous surface. How can spontaneous water flow occur for an intrinsic contact angle of 38°, which causes only partial wetting? Calculating the change of Free Energy dF for a small film advance dx on a rough surface yields $dF < 0$ for contact angles smaller than $\theta_c = \arccos(1/r)$, where the roughness r is the ratio of rough to flat surface. For a typical roughness of the glass ceramic of 1.5 (roughness parameter: $\delta = 1$, $\lambda = 2$ μm) the critical contact angle for complete wetting is 56°, that is, for an intrinsic contact angle of 38° the complete wetting condition is satisfied. The TFF-front advance follows a $\sqrt{(t)}$ behavior (Zulfiqar et al., 2020) as suggested by Bico et al. (2001). In conclusion, the dynamics on 2D sand analogs with rough surfaces are controlled by the temporal sequence/hierarchy of TFF and CF. Thick-film flow occurs first, followed by CF fed by TFF not by bulk/duct flow (see Video S1). Then throat instabilities and snap-offs occur at random positions (random bond occupation, such as *OP*). It is interesting that our micromodel experiments proved that precursor TFF and CF triggers snap-off trapping during *OP* and core annular flow triggers bypass trapping during IP. This interesting phase transition from wIP to OP is shown in Figure 2b.

Because the approach to the percolation threshold is universal, it depends only on the space dimension, and not on the network structure (Blunt & Scher, 1995; Geistlinger & Mohammadian, 2015; Geistlinger et al., 2019; Stauffer & Aharony, 1994; Wilkinson, 1984). At the percolation threshold p_c (or the terminal point, at which the non-wetting fluid becomes disconnected, Blunt & Scher, 1995), and for large cluster sizes s, the cluster probability
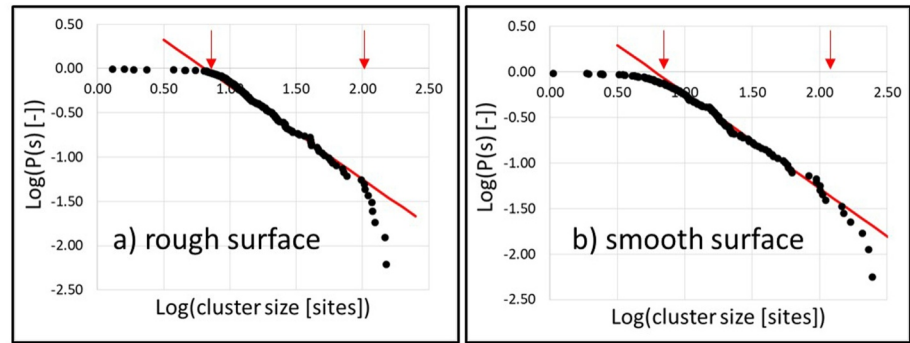
Figure 11. Universal scaling observed from the complementary cumulative probability function versus cluster size for 2D sand analog micromodels with (a) rough and (b) smooth surface. For clusters larger than the critical size (first red arrow) the size distribution follows a power law with a critical exponent $\tau = 2.05$ (slope of the red line is τ-1). Second red arrow marks data where finite size effects become significant.

(cluster size distribution) follows a universal power law decay with the Fisher exponent $\tau_{2D} = 2.05$ (Fisher, 1967; Stauffer & Aharony, 1994):

$$PDF(s, p_c) = n(s) = s^{-\tau}, \quad s \gg 1 \tag{4}$$

The complementary cumulative probability is defined as

$$P(s) = \text{CDF}(s_{\max}) - \text{CDF}(s)) = a \cdot s^{-b}(1 - \delta), \tag{5}$$

where $\text{CDF}(s)$ is the cumulative probability, $b = \tau - 1 = 1.05$, and $s_{\max}$ the maximal cluster size. For infinite cluster size $s_{\max} \to \infty$ the residual function $\delta \simeq s/s_{\max}$ vanishes, and $\log(P(s))$ shows a linear decrease with $\log(s)$. For finite $s_{\max}$ this linear behavior shows a deviation (finite size effect; compare with the experimental results for sandstones (Andrew et al., 2014b)):

$$\log(P(s)) = \tilde{a} - b \cdot \log(s) - \frac{s}{s_{\max}}, \quad s < s_{\max} \tag{6}$$

where it was assumed that δ is a small quantity, such that $\log(1 - \delta) \simeq -\delta$. Hence, the log-log representation elucidates the linear behavior that is, the universal power law only for cluster sizes large enough to be near the percolation threshold and small enough to exclude finite size effects. Figure 11 shows that for both 2D sand analogs at normal imbibition the cluster size distribution follows a power law with a critical exponent 2.05 (straight red line). All studied microstructures, whose flow regime is controlled by either IP or Ordinary percolation, show universal scaling (see Figure S8 in Supporting Information S1).

5. Conclusions

In summary, we have experimentally studied the displacement and trapping process in 2D and 3D porous media, when one fluid is displaced by another fluid in the capillary flow regime. Different phase transitions were observed with increasing contact angle, pore-scale heterogeneity/disorder, and surface roughness. They can be classified according to Blunt's phase diagram.

(i) Frontal Advance: For 2D and 3D glass beads that is, for uniform porous media with smooth surfaces, full duct flow and compact displacement cause no trapping during imbibition. With increasing contact angle, fractal displacement and bypass trapping occurs, that is, the flow system undergoes a phase transition to IP. The trapping efficiency increases from zero to maximal trapping. Both the 2D–3D trapped clusters show Universal Scaling that is, their size distribution follows a power law with a universal exponent of 2.05–2.19, respectively.

(ii) Ordinary percolation with trapping: For 2D–3D sand that is, for porous media with rough surfaces, spontaneous TFF with subsequent CF causes efficient snap-off events and leads to maximal trapping efficiency

during imbibition (3D: 13% trapping; 2D: 73% trapping). With an increasing contact angle, the trapping efficiency decreases to a minimum at neutral wettability (3D: zero trapping; 2D: 20% trapping) and increases again for strong drainage. Bypass trapping is caused here by core annular flow with an apparent contact angle of 180°. Consequently, the trapping efficiency shows a non-monotonous behavior. The trapping process during imbibition follows Ordinary percolation rules, where the snap-off events are triggered by precursor TFF and CF. The trapped clusters show Universal Scaling both in 2D and 3D.

Our findings also allow us to propose a plausible explanation to an intriguing question: Why the trapping efficiencies of five different rock samples examined in Andrew et al. (2014b) do not exhibit strong dependence on wettability, pore space morphology and topology? All these rock samples have highly irregular pore space with a similar degree of heterogeneity/disorder, pore size distribution and connectivity (except Mt Ganbier carbonate). We hypothesize that this is due to the fact that natural rocks are characterized by a significant surface roughness, which makes their intrinsic contact angle smaller than the critical contact angle ($\sim 60°$, Wenzel, 1936), and thus exhibit complete wetting, with spontaneous TFF. This results in *OP* with efficient snap-off trapping, explaining the high trapping efficiency and its relative insensitivity to wettability and pore space morphology and topology. However, neither *OP* with trapping nor the universal scaling of cluster sizes were observed for the Mt Gambier sample, suggesting that sample is not statistically representative. That is, finite size effects become important for that sample due to the very large clusters.

Finally, the fundamental understanding of trapping in this study was achieved for simpler settings that in some geologic applications, where the medium is often mixed- or fractional-wet (due to mineralogy, Geistlinger et al., 2020) and the flow rate could be higher than in the capillary regime (e.g., near wells in CO_2 injection). It would be interesting to extend the presented work to consider these more complicated cases. Nonetheless, we believe that our conclusions could be generalized to more complex cases, as we expect that the competition between flow through pore centers and along crevices and corners will continue to control trapping.

Data Availability Statement

The data on which this article is based are available in Geistlinger et al. (2023). Other micromodel data are available through Golmohammadi et al. (2021) and CT-data through Zulfiqar et al. (2020).

References

Adler, P. M., & Brenner, H. (1988). Multiphase flow in porous media. *Annual Review of Fluid Mechanics*, *20*(1), 35–59. https://doi.org/10.1146/annurev.fl.20.010188.000343

Akbarabadi, M., & Piri, M. (2013). Relative permeability hysteresis and capillary trapping characteristics of supercritical CO_2/brine systems: An experimental study at reservoir conditions. *Advances in Water Resources*, *52*, 190–206. https://doi.org/10.1016/j.advwatres.2012.06.014

AlRatrout, A., Blunt, M. J., & Bijeljic, B. (2018). Wettability in complex porous materials, the mixed-wet state, and its relationship to surface roughness. *Proceedings of the National Academy of Sciences*, *115*(36), 8901–8906. https://doi.org/10.1073/pnas.1803734115

Anbari, A., Chien, H.-T., Datta, S. S., Deng, W., Weitz, D. A., & Fan, J. (2018). Microfluidic model porous media: Fabrication and applications. *Small*, *14*(18), 1703575. https://doi.org/10.1002/smll.201703575

Andrew, M., Bijeljic, B., & Blunt, M. J. (2014a). Pore-scale contact angle measurements at reservoir conditions using X-ray microtomography. *Advances in Water Resources*, *68*, 24–31. https://doi.org/10.1016/j.advwatres.2014.02.014

Andrew, M., Bijeljic, B., & Blunt, M. J. (2014b). Pore-scale imaging of trapped supercritical carbon dioxide in sandstones and carbonates. *International Journal of Greenhouse Gas Control*, *22*, 1–14. https://doi.org/10.1016/j.ijggc.2013.12.018

Armstrong, R. T., & Wildenschild, D. (2012). Microbial enhanced oil recovery in fractional-wet systems: A pore-scale investigation. *Transport in Porous Media*, *92*(3), 819–835. https://doi.org/10.1007/s11242-011-9934-3

Bico, J., Tordeux, C., & Quéré, D. (2001). Rough wetting. *EPL (Europhysics Letters)*, *55*(2), 214–220. https://doi.org/10.1209/epl/i2001-00402-x

Blunt, M. J. (2017). *Multiphase flow in permeable media: A pore-scale perspective*. Cambridge University Press.

Blunt, M. J., & Scher, H. (1995). Pore-level modeling of wetting. *Physical review E*, *52*(6), 6387–6403. https://doi.org/10.1103/PhysRevE.52.6387

Bruecher, M., & Bottlinger, M. (2006). Dreidimensionale computersimulation zur untersuchung von partikelschüttungen aus unregelmäßig geformten partikeln. *Chemie Ingenieur Technik*, *78*(6), 727–733. https://doi.org/10.1002/cite.200500185

Cieplak, M., & Robbins, M. O. (1988). Dynamical transition in quasistatic fluid invasion in porous media. *Physical Review Letters*, *60*(20), 2042–2045. https://doi.org/10.1103/PhysRevLett.60.2042

Cieplak, M., & Robbins, M. O. (1990). Influence of contact angle on quasistatic fluid invasion of porous media. *Physical Review B*, *41*(16), 11508–11521. https://doi.org/10.1103/PhysRevB.41.11508

de Gennes PG, Q. D., & Brochard-Wyart, F. (2004). *Capillarity and wetting phenomena*. Springer. https://doi.org/10.1017/9781316145098

Delaunay, B. (1934). Sur la sphere vide. *Izv. Akad. Nauk SSSR, Otdelenie Matematicheskii i Estestvennyka Nauk*, *7*(793–800), 1–2. https://doi.org/10.4236/sar.2016.43003

El-Maghraby, R. M., & Blunt, M. J. (2013). Residual CO_2 trapping in Indiana limestone. *Environmental Science and Technology*, *47*(1), 227–233. https://doi.org/10.1021/es304166u

Fasshauer, G. E. (2007). *Meshfree approximation methods with matlab*. World Scientific. https://doi.org/10.1142/6437

Fisher, M. E. (1967). The theory of condensation and the critical point. *Physics Physique Fizika*, *3*(5), 255–283. https://doi.org/10.1103/PhysicsPhysiqueFizika.3.255

Furuberg, L., Feder, J., Aharony, A., & Jøssang, T. (1988). Dynamics of invasion percolation. *Physical Review Letters*, *61*(18), 2117–2120. https://doi.org/10.1103/PhysRevLett.61.2117

Geistlinger, H., & Ataei-Dadavi, I. (2015). Influence of the heterogeneous wettability on capillary trapping in glass-beads monolayers: Comparison between experiments and the invasion percolation theory. *Journal of Colloid and Interface Science*, *459*, 230–240. https://doi.org/10.1016/j.jcis.2015.07.074

Geistlinger, H., Ataei-Dadavi, I., Mohammadian, S., & Vogel, H.-J. (2015). The impact of pore structure and surface roughness on capillary trapping for 2-D and 3-D porous media: Comparison with percolation theory. *Water Resources Research*, *51*(11), 9094–9111. https://doi.org/10.1002/2015WR017852

Geistlinger, H., Ataei-Dadavi, I., & Vogel, H.-J. (2016). Impact of surface roughness on capillary trapping using 2d-micromodel visualization experiments. *Transport in Porous Media*, *112*(1), 207–227. https://doi.org/10.1007/s11242-016-0641-y

Geistlinger, H., Ding, Y., Apelt, B., Schlüter, S., Küchler, M., Reuter, D., et al. (2019). Evaporation study based on micromodel experiments: Comparison of theory and experiment. *Water Resources Research*, *55*(8), 6653–6672. https://doi.org/10.1029/2018WR024647

Geistlinger, H., Golmohammadi, S., Zulfiqar, B., Schlueter, S., Segre, E., & Holtzman, R. (2023). The interplay between pore-scale heterogeneity, surface roughness and wettability controls trapping in two-phase fluid displacement in porous media [Dataset]. *Figshare*, *51*(1). e2023GL106197. https://doi.org/10.6084/m9.figshare.24486598.v1

Geistlinger, H., & Mohammadian, S. (2015). Capillary trapping mechanism in strongly water wet systems: Comparison between experiment and percolation theory. *Advances in Water Resources*, *79*, 35–50. https://doi.org/10.1016/j.advwatres.2015.02.010

Geistlinger, H., & Zulfiqar, B. (2020). The impact of wettability and surface roughness on fluid displacement and capillary trapping in 2-D and 3-D porous media: 1. Wettability-controlled phase transition of trapping efficiency in glass beads packs. *Water Resources Research*, *56*(10), e2019WR026826. https://doi.org/10.1029/2019WR026826

Geistlinger, H., Zulfiqar, B., & Amro, M. (2020). New structural percolation transition in fractional wet 3D porous media: A μ-ct study. *Water Resources Research*, *56*(10), e2019WR026826. https://doi.org/10.1029/2021WR030037

Gogoi, S., & Gogoi, S. B. (2019). Review on microfluidic studies for eor application. *Journal of Petroleum Exploration and Production Technology*, *9*(3), 2263–2277. https://doi.org/10.1007/s13202-019-0610-4

Golmohammadi, S., Ding, Y., Kuechler, M., Reuter, S., Amro, M., & Geistlinger, H. (2021). Impact of wettability and gravity on fluid displacement and trapping in representative 2D micromodels of porous media (2D sand analogs) [Dataset]. *Water Resources Research*, *57*(10), 6653–6672. https://doi.org/10.1029/2021WR029908

Haghighi, M., Xu, B., & Yortsos, Y. (1994). Visualization and simulation of immiscible displacement in fractured systems using micromodels: I. Drainage. *Journal of Colloid and Interface Science*, *166*(1), 168–179. https://doi.org/10.1006/jcis.1994.1283

Herring, A. L., Sheppard, A., Andersson, L., & Wildenschild, D. (2016). Impact of wettability alteration on 3D nonwetting phase trapping and transport. *International Journal of Greenhouse Gas Control*, *46*, 175–186. https://doi.org/10.1016/j.ijggc.2015.12.026

Holtzman, R., & Segre, E. (2015). Wettability stabilizes fluid invasion into porous media via nonlocal, cooperative pore filling. *Physical review letters*, *115*(16), 164501. https://doi.org/10.1103/PhysRevLett.115.164501

Hu, R., Wan, J., Kim, Y., & Tokunaga, T. K. (2017). Wettability impact on supercritical CO_2 capillary trapping: Pore-scale visualization and quantification. *Water Resources Research*, *53*(8), 6377–6394. https://doi.org/10.1002/2017WR020721

Iglauer, S., Fernø, M., Shearing, P., & Blunt, M. (2012). Comparison of residual oil cluster size distribution, morphology and saturation in oil-wet and water-wet sandstone. *Journal of Colloid and Interface Science*, *375*(1), 187–192. https://doi.org/10.1016/j.jcis.2012.02.025

Juanes, R., Meng, Y., & Primkulov, B. K. (2020). Multiphase flow and granular mechanics. *Physical Review Fluids*, *5*(11), 110516. https://doi.org/10.1103/PhysRevFluids.5.110516

Jung, M., Brinkmann, M., Seemann, R., Hiller, T., de La Lama, M. S., & Herminghaus, S. (2016). Wettability controls slow immiscible displacement through local interfacial instabilities. *Physical Review Fluids*, *1*(7), 074202. https://doi.org/10.1103/PhysRevFluids.1.074202

Karadimitriou, N., & Hassanizadeh, S. (2012). A review of micromodels and their use in two-phase flow studies. *Vadose Zone Journal*, *11*(3), vzj20110072. https://doi.org/10.2136/vzj2011.0072

Lenormand, R., Touboul, E., & Zarcone, C. (1988). Numerical models and experiments on immiscible displacements in porous media. *Journal of Fluid Mechanics*, *189*, 165–187. https://doi.org/10.1017/S0022112088000953

Lenormand, R., & Zarcone, C. (1984). Role of roughness and edges during imbibition in square capillaries. In *SPE annual technical conference and exhibition*. https://doi.org/10.2118/13264-MS

Lenormand, R., & Zarcone, C. (1985). Invasion percolation in an etched network: Measurement of a fractal dimension. *Physical Review Letters*, *54*(20), 2226–2229. https://doi.org/10.1103/physrevlett.54.2226

Patsoukis Dimou, A., Menke, H. P., & Maes, J. (2022). Benchmarking the viability of 3D printed micromodels for single phase flow using particle image velocimetry and direct numerical simulations. *Transport in Porous Media*, *141*(2), 1–16. https://doi.org/10.1007/s11242-021-01718-8

Pentland, C. H., El-Maghraby, R., Iglauer, S., & Blunt, M. J. (2011). Measurements of the capillary trapping of super-critical carbon dioxide in berea sandstone. *Geophysical Research Letters*, *38*(6), L06401. https://doi.org/10.1029/2011gl046683

Primkulov, B. K., Pahlavan, A. A., Fu, X., Zhao, B., MacMinn, C. W., & Juanes, R. (2021). Wettability and lenormand's diagram. *Journal of Fluid Mechanics*, *923*, A34. https://doi.org/10.1017/jfm.2021.579

Rabbani, H. S., Joekar-Niasar, V., Pak, T., & Shokri, N. (2017). New insights on the complex dynamics of two-phase flow in porous media under intermediate-wet conditions. *Scientific Reports*, *7*(1), 1–7. https://doi.org/10.1038/s41598-017-04545-4

Rahman, T., Lebedev, M., Barifcani, A., & Iglauer, S. (2016). Residual trapping of supercritical CO_2 in oil-wet sandstone. *Journal of Colloid and Interface Science*, *469*, 63–68. https://doi.org/10.1016/j.jcis.2016.02.020

Schindelin, J., Arganda-Carreras, I., Frise, E., Kaynig, V., Longair, M., Pietzsch, T., et al. (2012). Fiji: An open-source platform for biological-image analysis. *Nature Methods*, *9*(7), 676–682. https://doi.org/10.1038/nmeth.2019

Schlüter, S., Weller, U., & Vogel, H.-J. (2010). Segmentation of X-ray microtomography images of soil using gradient masks. *Computers and Geosciences*, *36*(10), 1246–1251. https://doi.org/10.1016/j.cageo.2010.02.007

Singh, K., Scholl, H., Brinkmann, M., Michiel, M. D., Scheel, M., Herminghaus, S., & Seemann, R. (2017). The role of local instabilities in fluid invasion into permeable media. *Scientific Reports*, *7*(1), 1–11. https://doi.org/10.1038/s41598-017-00191-y

Stauffer, D., & Aharony, A. (1994). *Introduction to percolation theory*. Taylor and Francis. https://doi.org/10.1201/9781315274386

Trojer, M., Szulczewski, M. L., & Juanes, R. (2015). Stabilizing fluid-fluid displacements in porous media through wettability alteration. *Physical Review Applied*, *3*(5), 054008. https://doi.org/10.1103/PhysRevApplied.3.054008

Wenzel, R. N. (1936). Resistance of solid surfaces to wetting by water. *Industrial and Engineering Chemistry*, *28*(8), 988–994. https://doi.org/10.1021/ie50320a024

Wildenschild, D., Armstrong, R. T., Herring, A. L., Young, I. M., & Carey, J. W. (2011). Exploring capillary trapping efficiency as a function of interfacial tension, viscosity, and flow rate. *Energy Procedia*, *4*, 4945–4952. https://doi.org/10.1016/j.egypro.2011.02.464

Wilkinson, D. (1984). Percolation model of immiscible displacement in the presence of buoyancy forces. *Physical Review A*, *30*(1), 520–531. https://doi.org/10.1103/PhysRevA.30.520

Xu, W., Ok, J. T., Xiao, F., Neeves, K. B., & Yin, X. (2014). Effect of pore geometry and interfacial tension on water-oil displacement efficiency in oil-wet microfluidic porous media analogs. *Physics of Fluids*, *26*(9), 093102. https://doi.org/10.1063/1.4894071

Zhao, B., MacMinn, C. W., & Juanes, R. (2016). Wettability control on multiphase flow in patterned microfluidics. *Proceedings of the National Academy of Sciences*, *113*(37), 10251–10256. https://doi.org/10.1073/pnas.1603387113

Zhao, B., MacMinn, C. W., Primkulov, B. K., Chen, Y., Valocchi, A. J., Zhao, J., et al. (2019). Comprehensive comparison of pore-scale models for multiphase flow in porous media. *Proceedings of the National Academy of Sciences*, *116*(28), 13799–13806. https://doi.org/10.1073/pnas.1901619116

Zulfiqar, B., Vogel, H., Ding, Y., Golmohammadi, S., Küchler, M., Reuter, D., & Geistlinger, H. (2020). The impact of wettability and surface roughness on fluid displacement and capillary trapping in 2-D and 3-D porous media: 2. Combined effect of wettability, surface roughness, and pore space structure on trapping efficiency in sand packs and micromodels [Dataset]. *Water Resources Research*, *56*(10), e2020WR027965. https://doi.org/10.1029/2020WR027965

Zuo, L., Zhang, C., Falta, R. W., & Benson, S. M. (2013). Micromodel investigations of CO_2 exsolution from carbonated water in sedimentary rocks. *Advances in Water Resources*, *53*, 188–197. https://doi.org/10.1016/j.advwatres.2012.11.004

References From the Supporting Information

Geistlinger, H., & Mohammadian, S. (2015). Capillary trapping mechanism in strongly water wet systems: Comparison between experiment and percolation theory. *Advances in Water Resources*, *79*, 35.

Küchler, M., Otto, T., Gessner, T., Ebling, F., & Schroder, H. (2003). Hot embossing for mems using silicon tools. *International Journal of Computational Engineering Science*, *4*, 609.